Retrieval of UVB aerosol extinction profiles from the ground-based Langley Mobile Ozone Lidar (LMOL) system

Liqiao Lei[1,2], Timothy A. Berkoff[2], Guillaume Gronoff [2,3], Jia Su[4], Amin R. Nehrir[2], Yonghua Wu[5,6], Fred Moshary[5,6], Shi Kuang[7]

[1]Universities Space Research Association, Columbia, MD, USA
[2]NASA Langley Research Center, Hampton, VA, USA
[3]Science Systems and Applications, Hampton, VA, USA
[4]Hampton University, Hampton, VA, USA
[5]City College of New York (CCNY), New York, NY 10031, USA
[6]NOAA – Cooperative Science Center for Earth System Sciences and Remote Sensing Technologies, USA
[7]University of Alabama in Huntsville, Huntsville, Alabama, USA

Correspondence to: Liqiao Lei (liqiaolei1007@gmail.com)

Abstract. Aerosols emitted from wildfires are becoming one of the main sources of poor air quality in the US mainland. Their extinction in UVB (wavelength range 280-315 nm) is difficult to be retrieved using simple lidar techniques because of the impact of O_3 absorption and the lack of data about the lidar ratios at those wavelengths. Improving the characterization at these wavelengths will enable their monitoring with different instruments and also will permit to correct the aerosol impact on the ozone lidar data. The 2018 Long Island Sound Tropospheric Ozone Study (LISTOS) campaign in the New York City region brought a comprehensive set of instruments that enabled the characterization of lidar ratio for UVB aerosol retrieval. The NASA Langley High Altitude Lidar Observatory (HALO) produced the 532 nm aerosol extinction product along with the lidar ratio for this wavelength by using a high spectral resolution technique. The Langley Mobile Ozone Lidar (LMOL) is able to compute the extinction provided it has the lidar ratio at 292nm. The lidar ratio at 292nm and the Ångström Exponent (AE) between 292 nm and 532nm for the aerosols were retrieved by comparing the two observations using an optimization technique. We evaluate the aerosol extinction error due to the selection of these parameters, usually done empirically for 292nm lasers. This is the first known 292nm aerosol product inter-comparison between HALO and Tropospheric Ozone Lidar Network (TOLNet) ozone lidar. It also provided the characterization of the UVB optical properties of aerosol in the lower troposphere affected by transported wildfire emission.

1 Introduction

Wildfires produce substantial amounts of gaseous pollutants such as carbon monoxide (CO), nitrogen oxides (NO_x), volatile organic compounds (VOCs), and ozone (O_3) as well as biomass burning particulate which significantly impact the climate and air quality (Andreae and Merlet, 2001; Phuleria et al., 2005; Reid et al., 2005; Zauscher et al., 2013). Pollutants directly emitted from wildfire can affect first responders and local residents. In addition, transported wildfire emission can lead to harmful exposures for populations in regions far away from the wildfires (Cottle et al., 2014; Dreessen et al., 2016). The increase in frequency and severity of North American wildfires significantly affects air quality by increasing the amount of particulates and ozone in the air (Schoennagel et al., 2017). Ground-based lidars have the ability of simultaneously detecting O_3 and aerosol with high temporal and vertical resolution to better understand air quality exceedances that can be exacerbated by transported wildfire emission (Aggarwal et al., 2018; Strawbridge et al., 2018; Kuang et al., 2020). On the other hand, the determination of the aerosol properties in UVB wavelength region is of great importance to understand the effect of aerosol on UV radiation which is linked to human health and atmospheric chemistry (Bais et al., 1993; Carlund et al., 2017; Moozhipurath and Skiera, 2020). Lidar aerosol measurements at 355 nm are often reported, but the UVB aerosol properties are rarely studied by lidar (Müller et al., 2007; Nicolae et al., 2013; Haarig et al., 2018). To bridge that gap in our understanding of the impact of transported wildfire emission on air quality and the aerosol optical properties in UVB band, this work describes a technique to retrieve the aerosol extinction at 292 nm by comparing the data from a UV-lidar along with the data from a High Spectral Resolution Lidar (HSRL).

Retrieval and validation of lidar aerosol profiles in the UVB wavelengths range are challenging due to 3 factors.

First, strong O_3 absorption at UVB wavelengths can cause large uncertainty for retrieval of UVB aerosol. One approach to address this is to use O_3 measurements to correct the O_3 absorption before the extinction/backscatter retrieval technique is applied (Browell 1985; Young, 1995).

Second, the aerosol extinction to backscatter ratio, also known as the lidar ratio, noted S_1, is not well known for different aerosol types at UVB wavelengths. In general, a relative S_1 is needed to retrieve an accurate UVB aerosol profile. For example, Kuang et al. (2020) demonstrated retrieval of aerosol 299 nm backscatter from the ozone lidar raw attenuated backscatter signal using an iteration algorithm and fixed S_1 (60 sr) in the presence of smoke. However, it will introduce uncertainty for the aerosol retrieval if we use one S_1 value for aerosol with different type because S_1 is dependent upon the aerosol type and can exhibit values between approximatively 10 and 90 (Omar et al., 2009; Lopes et al., 2013, Müller et al., 2007; Burton et al., 2014; Haarig et al., 2018). An accurate S_1 at UVB wavelength range is needed to obtain a realistic UVB aerosol profile retrieval.

Finally, the lack of available aerosol profiles at UVB wavelength range to validate the retrieved aerosol result. However, aerosol profiles provided by a more common 532nm/355nm aerosol lidar could be used for validation if the Ångström Exponent (AE) between the UVB wavelength and 532nm/355nm is available. This work will focus on addressing these 3 factors and retrieve aerosol extinction at 292 nm for Langley Mobile Ozone Lidar (LMOL) system.

The Long Island Sound Tropospheric Ozone Study (LISTOS) campaign was a multi-agency collaborative study for the areas of Long Island Sound and surrounding coastlines in summer 2018 that provided the perfect conditions to perform that work. The LMOL and the airborne NASA Langley High Altitude Lidar Observatory (HALO) system were both operating during the LISTOS campaign. HALO provided the extinction and the S_1 value at 532nm thanks to a High Resolution Spectroscopy Lidar (HSRL) technique. As figure s1 shows, the HALO overpasses over LMOL enabled coincident measurements which in turn allowed the characterization of the aerosols S_1 and AE (292nm and 532 nm) as explained in section 3. The information about lidar ratio at 292 nm and AE (292 nm and 532 nm) not only improve our UV aerosol retrieval, but also improve our understanding of the aerosol optical properties at those wavelengths. During the LISTOS campaign, the case study of August 2018 was selected as an example of the UVB aerosol retrieval because HALO/LMOL coincident aerosol data but also because of the air quality exceedance probably caused by the impact of long-range transport of wildfire emissions (Rogers et al., 2020). The evaluation of the aerosols optical properties allows to better validate their age and therefore their wildfire origin when compared to back trajectories.

The instruments and data used in this work are described in the next section. We use the LMOL raw and O_3 data products, HALO aerosol backscatter/extinction and S_1 data, the City College of New York (CCNY) 532 nm aerosol extinction data, and the CL51 backscatter data. The method to retrieve UVB aerosol extinction, as well as the method to select the optimized S_1 for UVB aerosol retrieval is presented in section 3 (Step A to C in figure 1). The comparison between the retrieved LMOL aerosol extinction profile and the HALO aerosol extinction profile using the optimized parameter are presented in section 4. The retrieved LMOL aerosol extinction comparison with the CL51 and CCNY aerosol lidar data is also presented in section 4. The uncertainty for the aerosol extinction retrieval is analysed in section 5. Finally, the importance of this method is discussed in Section 6.2 Instrument and data

2 Instrument and data

2.1 The LMOL system

LMOL is a mobile ground-based O_3 differential absorption lidar (DIAL) system that has a transmitter with a 1 kHz diode-pumped Q-switched Nd:YLF 527 nm laser to pump a custom-built Ce:LiCAF tunable UV laser to generate “on” and “off” DIAL wavelengths at 286 nm and 292 nm. A 40 cm diameter telescope was used to collect the back scatter signal for the far-field and a smaller diameter wide field off-axis parabolic mirror is used for the near-field return (De Young et al., 2017; Farris et al., 2019). Both far-field and near-field receiver channels employ analog and photon detection modes using a high-speed Licel data acquisition system to maximize measurement dynamic range. The current configuration of LMOL can retrieve O_3 profiles from 0.1 to 10 km range at night, with 5 to 10-minute temporal averaging (Gronoff et al. 2019, 2021, Farris et al., 2019). During daytime, the maximum altitude reached is typically close to 5 km due to solar background light limitations. LMOL is part of Tropospheric Ozone Lidar Network (TOLNet) (https://www-air.larc.nasa.gov/missions/TOLNet/), a network of O_3 lidars that help evaluate air quality models and compliment current and planned satellite retrievals for satellite such as

the Tropospheric Emissions: Monitoring of Pollution (TEMPO) mission (Zoogman et al., 2017). LMOL generates data products following the TOLNet protocol for the acquisition, processing, and archiving of the data that assure the quality and consistency of the data products (Leblanc et al., 2016a; Leblanc et al., 2016b; Leblanc et al.,2018). For LMOL data products, the vertical resolution (110 m to 990m) of the O_3 profiles varies with altitude to preserve a retrieval uncertainty within $\pm$10%, the uncertainty of which is calculated using poison statistics of the backscattered photons. LMOL has been used in several campaigns such as Ozone Water-Land Environmental Transition Study (OWLETS) I and II, LISTOS (*Berkoff et al.*,2018; *Sullivan et al.,* 2019; *Dacic et al.*, 2020), Fire Influence on Regional to Global Environments and Air Quality (FIREX-AQ), and Southern California Ozone Observation Project (SCOOP) (Leblanc et al., 2018). In the context of LISTOS (Wu et al., 2021), and more specifically for the present study, LMOL was deployed at Sherwood Island Park, Westport, CT (41.1182° N, 73.3368° W, 2.5 m ASL) and obtained measurements between July 12 and August 29, 2018. To obtain the aerosol products, we used the LMOL raw data at 292nm and the LMOL O_3 data.

2.2 The Ceilometer located nearby LMOL

A ceilometer (Vaisala CL51) was installed at the Westport site co-located with LMOL at 41.1173N, 73.3369 W, 3 m above sea level during the LISTOS campaign. A ceilometer is a single-wavelength backscatter lidar system used to monitor cloud base height and aerosol structures (Wang et al., 2018). A semiconductor laser (InGaAs diode laser) with 3.0 uJ pulse energy and repetition rate of 6.5 kHz retrieves the atmospheric backscatter at 910 nm to infer the vertical distribution of clouds and aerosols up to 15 km (Lee et al., 2018; Jin et al., 2015). The measured backscatter signal was integrated over 5 seconds. It is an autonomous eye-safe system which obtains measurements makes 24-hr/7-day observations. Although the molecular signal returns are weak because of the low-energy laser and the near-infrared wavelength, the stronger returns from aerosols and clouds can be detected. The CL51 signal is impacted by dark current noise and daytime solar background, but still sufficient to measure signals from boundary layer aerosols up to 3 km (Jin et al., 2015). As a result, the ceilometer can provide the boundary layer evolution and aerosol retrievals up to 3 km to qualitatively compare with LMOL.

2.3 The HALO aerosol measurement

The NASA airborne High Altitude Lidar Observatory (HALO) is a combied High Spectral Resolution Lidar (HSRL) and H_2O and CH_4-differential absorption lidar (DIAL) (Nehrir et al., 2017; Wu et al., 2021). HALO employs 1 KHz Nd:YAG pumped optical parametric oscillators to generate the DIAL wavelength for H_2O and CH_4 observations. The residual energy from the conversion process is employed for the HSRL technique. HALO employs the HSRL technique at 532 nm, the backscatter technique at 1064nm, and measures depolarization at both 532/1064 nm. And I2 vapor cell is used to in the receiver to separate the molecular scattering from the total scattering (Hair et al., 2008). This allows for discrimination of aerosol scattering from molecular and retrieval of aerosol extinction and backscatter coefficient independently (Burton et al., 2013, 2014, 2015, Hair et al, 2008). The lidar extinction-to-backscatter ratio is then available from the HALO determined aerosol extinction and backscatter coefficients. HALO data are sampled at 0.5-s temporal and 1.25 m vertical resolution. This vertical resolution for

the aerosol measurement is increased to 15 m in post-processing to increase the SNR of the aerosol intensive and extensive retrievals. Aerosol backscatter and depolarization products are averged 10 s horizontally and aerosol extinction products are averaged 60 s horizontally and 150 m vertically. The polarization and HSRL gain ratios are calculated as described in Hair et al., 2008. Operational retrievals also provide mixing ratio of non-spherical -to-spherical backscatter (Sugimoto and Lee, 2006), aerosol type, (Burton et al., 2012) and aerosol mixed layer height (Scarino et al., 2014). In this study, the HALO aerosol extinction data are selected when its flight measurements are overpass the LMOL site.

2.4 The CCNY aerosol lidar

The CCNY lidar transmits 1064, 532, and 355 nm with a flash lamp-pumped Nd: YAG laser with a pulse repetition rate of 30 Hz. A telescope with 50 cm diameter collects three-wavelength elastic scatter and two Raman-scattering returns (by nitrogen and water vapor excited by 355 nm laser). The aerosol extinction and backscatter profiles in the troposphere were retrieved and the AE was derived to distinguish fine mode aerosol from coarse mode aerosol. CCNY lidar return signals detection start from 0.5 km with a 1-min time average and 3.75 m vertical data-bin resolution. The PBL height was estimated from the 1064 nm elastic return because the backscatter signal in this wavelength is more sensitive to aerosol structures than shorter wavelength (Wu et al., 2019; Wu et al., 2018, Wu et al. 2021). CCNY lidar was located at New York City (NYC) (40.8198° N, -73.9483° W) to remote sensing the aerosol layer aloft during the LISTOS campaign.

3 Methodology

It is important to determine the S_1 for LMOL 292 nm aerosol retrieval. The O_3 corrected LMOL attenuated backscatter profile does not contain information needed to estimate S_1. Fortunately, the HALO observations provide the 532 nm extinction and S_1 which could help us to learn some information about the aerosol optical properties for the cases where the two instruments have coincident observations.

To retrieve the S_1 , an iterative method with 3 main steps was used as shown in Figure 1. The first step is the retrieval of the aerosol extinction at 292nm from LMOL. For that, the LMOL raw data are corrected from the ozone absorption. Then the Fernald method is used with an empirical S_1 (which is modified in subsequent iterations to explore the parameter space). For the current study, the impact of the aerosols was low enough that an iterative correction to the O_3 density was not necessary to retrieve the aerosol extinction accurately; for dense aerosols layers, the method described in Browell et al., 1985 would have been used. The second step is the retrieval of the aerosol extinction at 292 nm from HALO. The conversion of the extinction from 532nm to 292nm is done by using an assumed AE (between 292 nm and 532 nm) which is also modified in subsequent iteration to explore the (S_1, AE) parameter space. The third step is the comparison of the aerosol extinction from both instruments at 292 nm. The integration of the difference provides the partial aerosol optical depth (AOD) difference, refered later as the partial AOD index. Once the plausible (S_1, AE) parameter space has been explored, there will be a minimum to the partial AOD index which points to the best (S_1, AE) for the observed conditions. The LMOL aerosol extinction profile related

to optimized S_1 and difference between the LMOL and HALO 292 nm aerosol profile related to the optimized S_1, and AE was also recorded for further analysis.

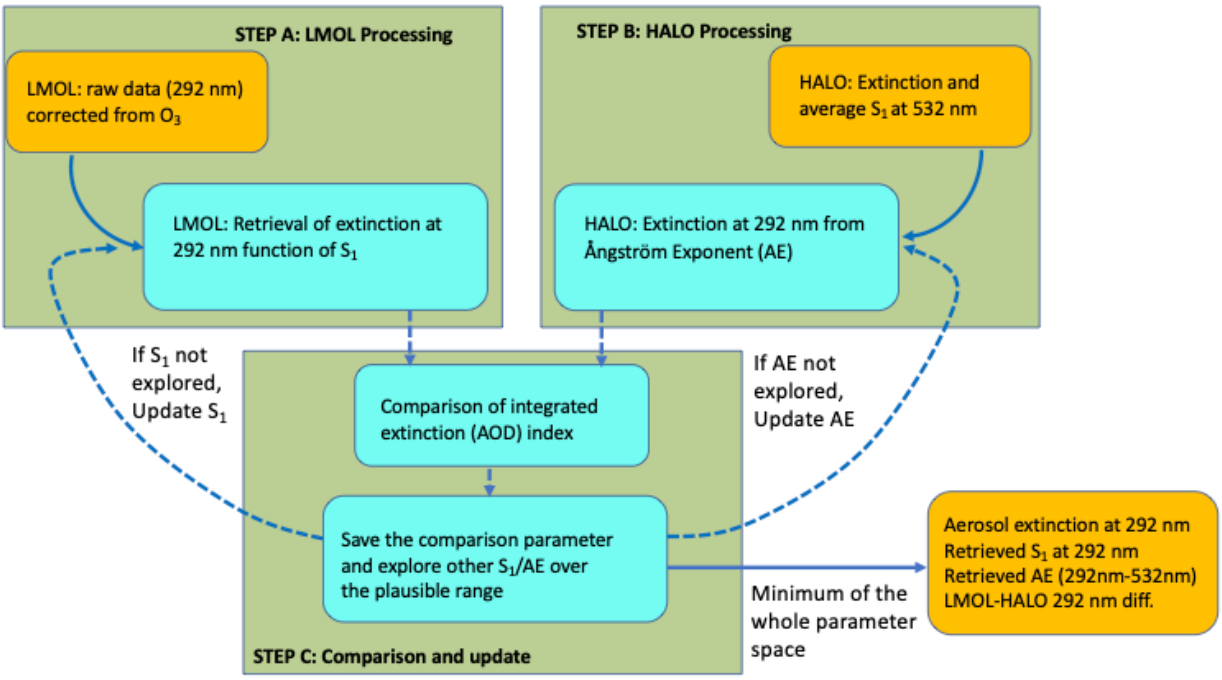

Figure 1. Flow chart for the approach used in this work. The cyan section corresponds to the processing needed for the retrieval of the optimal *(S_1, AE)*

3.1 Method to retrieve aerosol extinction coefficient

LMOL uses the 287 nm and 292 nm wavelengths for O_3 DIAL measurements. The 292 nm "off" wavelength was selected for the aerosol retrieval in this work because O_3 has a smaller absorption cross section at this wavelength. The attenuated lidar signal measured by the LMOL system can be represented by,

$$P_\lambda(R) = \frac{C_\lambda\left(\beta_{\lambda,a}(R)+\beta_{\lambda,m}(R)\right)\{\exp\left[-2\int_0^R\left(\alpha_{\lambda,a}(r)+\alpha_{\lambda,m}(r)+\sigma_{\lambda,O_3}N_{O_3}(r)\right)dr\right]\}}{R^2} + P_0 \quad (1)$$

where $P_\lambda(R)$ is lidar return signal power, λ is laser wavelength, C_λ is lidar system constant, $\beta_{\lambda,a}(R)$ is aerosol volume backscatter coefficient, $\beta_{\lambda,m}(R)$ is molecular volume backscatter coefficient, $\alpha_{\lambda,a}(R)$ is aerosol optical extinction coefficient, $\alpha_{\lambda,m}(R)$ is molecular optical extinction coefficient (without the O_3 extinction), σ_{λ,O_3} is the O_3 absorption cross section, $N_{O_3}(R)$ is the O_3 number density. $P_{\lambda,0}$ is the offset which contributed by the sky background signal, amplifier and digitizer offset, and

detector dark current (Fernald, 1984; Young et al., 2009). We also have $\alpha_{\lambda,m}(R) = \sigma_m N_m$ where σ_m is the atmospheric extinction cross section and N_m is the atmospheric molecular number density. The molecular extinction coefficient and backscatter coefficient are usually calculated from the balloon measurement close to the lidar site or from model like GEOS 5 (Sasano and Nakane, 1984).

The aerosol extinction-to-backscattering ratio (also known as lidar ratio) is $S_1 = \alpha_{\lambda,a}/\beta_{\lambda,a}$, and the molecular extinction-to-backscatter ratio is $S_2 = \alpha_{\lambda,m}/\beta_{\lambda,m} = 8\pi/3$ (Kovalev and Eichinger, 2004). The S_1 value is dependent on the particle size, shape, and refractive index, and usually varies from ~10 to 100 sr (Sasano and Nakane, 1984). We have assumed a constant S_1 with range for the aerosol extinction retrieval (Fernald, 1972; Fernald, 1984). The received LMOL lidar signal at 292 nm could be corrected with the ozone profile to get the elastic lidar attenuated backscatter signal attributed to aerosol and molecular terms as shown in equation (2). The O_3 corrected range-corrected lidar signal with background subtraction is shown as following:

$$\left[P_\lambda(R) - P_{\lambda,0}\right]R^2\{\exp\left[2\int_0^R \sigma_{\lambda,O_3}N_{O_3}(r)\,dr\right]\} = C_\lambda\left(\beta_{\lambda,a}(R) + \beta_{\lambda,m}(R)\right)\{\exp\left[-2\int_0^R\left(\alpha_{\lambda,a}(r) + \alpha_{\lambda,m}(r)\right)dr\right]\} \quad (2)$$

We can rearrange Equation (2) to get the aerosol attenuated backscatter signal X(R):

$$X(R) = C_\lambda\left(\beta_{\lambda,a}(R) + \beta_{\lambda,m}(R)\right)\{\exp\left[-2\int_0^R\left(\alpha_{\lambda,a}(r) + \alpha_{\lambda,m}(r)\right)dr\right] \quad (3)$$

where $X(R) = \left[P_\lambda(R) - P_0\right]R^2\{\exp\left[2\int_0^R \sigma_{\lambda,O_3}N_{O_3}(r)\,dr\right]\}$. Use equation (3) and the aerosol and molecular extinction-to-backscattering ratio, the aerosol extinction coefficient at ranges between the lidar and calibration range R_c is shown in equation (4) (Fernald, 1984; Sasano et al., 1985). The equations after here do not include λ for convenience.

$$\alpha_a(R) + \frac{S_1}{S_2}\alpha_m(R) = \frac{X(R)\{\exp\left[-2\left(\frac{S_1}{S_2}-1\right)\int_{R_c}^R \alpha_m(r)dr\right]\}}{\frac{X(R_C)}{\alpha_a(R_C)+\frac{S_1}{S_2}\alpha_m(R_C)} - 2\int_{R_c}^R X(r)\{\exp\left[-2\left(\frac{S_1}{S_2}-1\right)\int_{R_c}^r \alpha_m(r')dr'\right]\}dr} \quad (4)$$

In order to calculate the aerosol extinction coefficient $\alpha_a(R)$, we need to assume S_1 and the reference value of the aerosol extinction coefficient at a calibration range R_c. The reference value $\alpha_a(R_c)$ must be known or estimated. The calibration range and the reference value could be estimated use the secant method mentioned by Li et al, 2018. We need pay attention to that all data used in the aerosol retrieval process should has same vertical resolution. The retrieval is applied to cloud-free profiles after applying a cloud screening on the data. This was done by using the convolution of the O_3 corrected attenuated backscatter signal and a Harr wavelet function to identify cloud edges and then further screened by using a threshold to separate cloud features (Burton et al., 2010, Compton et al., 2013; Scarino et al., 2014). The aerosol extinction was retrieved for both LMOL far-field-photon-counting and far-field-analog signal channels. The near field aerosol retrieval will be described in a separate work. The aerosol extinction profiles for those two channels were merged to a single profile with overlapping altitude zone 1.5-2 km. The lowest altitude for the retrieved profile is about 0.5 km with the highest altitude for retrieved aerosol being constrained by the highest altitude of reliable O_3 data.

3.2 Selection of the UVB S_1 for retrieval

As mentioned in section 1, we focus on case studies from August 2018, especially during the afternoon period of August 28, 2018. The average S_1 for HALO at 532 nm S_1 profiles was calculated for August 28, 2018, afternoon data. The HALO S_1 mentioned hereafter are the vertically average S_1 derived from HALO S_1 profile. The frequency distribution of the HALO S_1 for the afternoon August 28, 2018, is shown in Figure 2 (a). The mean HALO S_1 for 532 nm is ~ 55 sr with a 1-s standard deviation ~3 sr. As figure 2 (b) show, the mean HALO S_1 for all available August measurement is ~55 with 1-s standard deviation ~6 sr. The HALO 532 nm S_1 data was screened by criteria of S_1 larger than 10 sr and less than 100 sr when calculating the average for each S_1 profile.

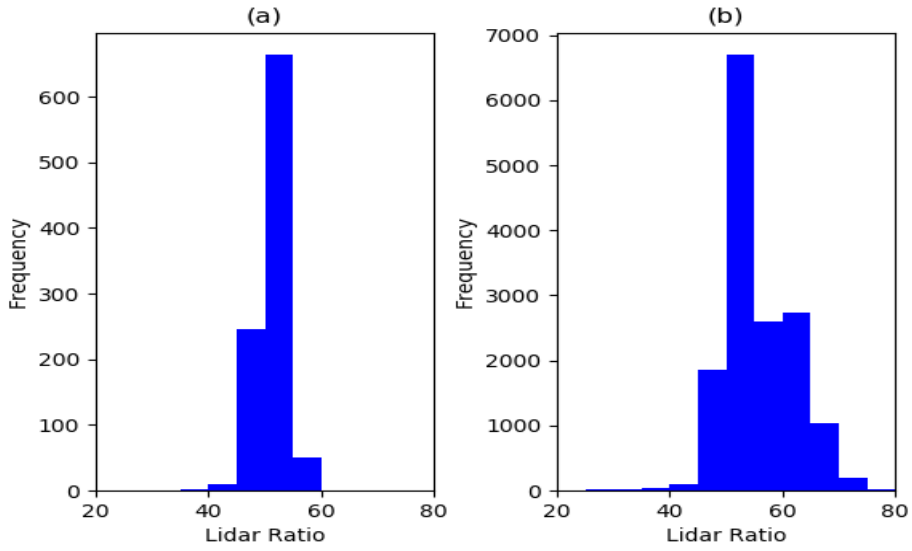

Figure 2: The histogram of average HALO S_1 frequency distribution for (a) August 28 afternoon, and (b) August 5, 6, 15, 16, 24, 28, and 29, 2018 measurement during LISTOS campaign.

The following paragraph will introduce the method to identify the S_1 at 292 nm and extinction AE between 292nm and 532nm by calculating the partial AOD difference between the retrieved LMOL 292 nm aerosol extinction profile and HALO aerosol extinction profile. The AE represents the wavelength dependency of the AOD or extinction coefficient for aerosol. The AE (noted as $\alpha_{\lambda_1,\lambda_2}$) between two wavelengths λ_1 and λ_2 is expressed as the following equation (Wagner and Silva, 2008):

$$\alpha_{\lambda_1,\lambda_2} = -\frac{\ln\left(\frac{\tau_1}{\tau_2}\right)}{\ln\left(\frac{\lambda_1}{\lambda_2}\right)} \quad (5)$$

where τ_1 and τ_2 are the AOD at wavelength λ_1 and λ_2.

The ideal S_1 at 292 nm and AE between 292 nm and 532 nm were determined from the retrieved LMOL aerosol extinction profiles and aerosol profiles provided by co-located HALO measurements using a partial AOD difference method. Figure 3 shows the flow chart for 5 steps of this partial AOD difference method. In step 1, the LMOL aerosol extinction was retrieved by incrementing $S_1(i)$ from 10 sr to 90 sr in steps of 5 sr and notes as $\alpha_{LMOL,S_1\,(i)}(R)$. Step 2, The LMOL aerosol extinction $\alpha_{LMOL,S_1\,(i)}(R)$ multiply ΔR (7m in this work) to get the LMOL partial AOD at altitude R which noted as $PAOD_{LMOL,S_1(i)}(R)$. Step 3, HALO 532 nm aerosol extinction was converted to aerosol extinction at 292 nm with AE (j) and varied from 0.5 to 2.5 with step 0.1. Then the 292nm HALO aerosol extinction $\alpha_{HALO,AE\,(j)}(R)$ is multiplied by ΔR to obtain the HALO partial AOD at altitude R which was noted as $PAOD_{HALO,AE(j)}(R)$. Step 4, the relative difference of partial AOD (noted as $\Delta PAOD_{i,j}(R)$) between $PAOD_{LMOL,S_1(i)}$(R) and $PAOD_{HALO,\ AE(j)}(R)$ was calculated using equation (6). Step 5, the $\Delta PAOD_{i,j}(R)$) were integrated to get the partial AOD difference index $PAODI(i,j)$ using equation (7). In equation (7), R_b and R_t is the bottom and top altitude for calculating the P$AODI(i,j)$.

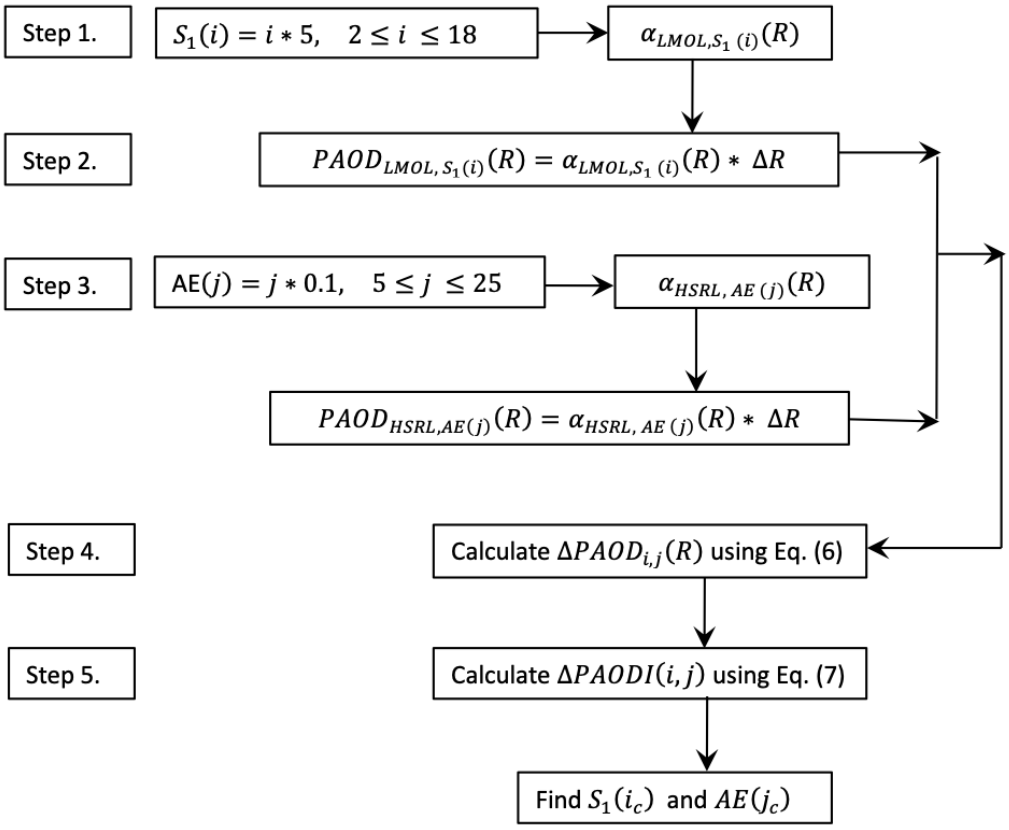

Figure 3: The flow chart for process of calculating the 292 nm S_1 and AE between 532 nm and 292 nm. "i" is the integer increment from 2 to 18 that used to calculate the S_1 to make the S_1 varies from 10 to 90. "j" is the integer increment from 5 to 25 that used to calculate the AE to make the AE varies from 0.5 to 2.5. "I" and "j" also could be the index of the calculated partial AOD.

The S_1(i), AE (j), *PAODI(i,j)*, corresponding LMOL 292 nm aerosol extinction profile, and the corresponding LMOL-HALO aerosol profile difference were all recorded. We use the S_1(i), AE (j), and *PAODI(i,j)* data to find the minimum *PAODI(i,j)* and corresponding S_1 and AE, which noted as $S_1(i_c)$ and $AE(j_c)$. The LMOL 292 nm aerosol extinction profile corresponding to $S_1(i_c)$ is the value for the LMOL aerosol retrieval. The LMOL-HALO aerosol profile difference corresponding to $S_1(i_c)$ and $AE(j_c)$ indicating the LMOL aerosol and HALO aerosol extinction comparison. This partial AOD difference method indicates the detail of how to calculate the optimized S_1, AE, and corresponding to the cyan section in figure 1.

$$\Delta PAOD_{i,j}(R) = \frac{abs\left[PAOD_{LMOL,S_1(i)}(R) - PAOD_{HALO,AE(j)}(R)\right]}{\left[(PAOD_{LMOL,S_1(i)}(R) + PAOD_{HALO,AE(j)}(R))/2\right]} \quad (6)$$

$$PAODI(i,j) = \sum_{R=R_b}^{R_t} \Delta PAOD_{i,j}(R) \quad (7)$$

In order to show how the PAODI changed with the 292 nm S_1 and the AE (292 & 532 nm), we further calculate the percentage relative difference of the PAODI compared with $PAODI_{min}$. An example of this partial AOD difference method at 13:17 EDT on August 28, 2018, was shown in figure 4. The PAODI was calculated for altitude regions from 0.5 to 3 km. The result in figure 4 (a) show that the selected S_1 is 35 sr and selected AE (292 & 532 nm) is 1.4. Therefore, the S_1 of 35 sr is the ideal choice for aerosol extinction retrieval on August 28, 2018, afternoon. As show in figure 4 (b) the LMOL S_1, and AE (292 & 532 nm) at (40, 1.5) and (30,1.3) also has PAODI value very close to $PAODI_{min}$ and could be potential choice for the LMOL retrieval and comparison. Significant errors can arise when improper S_1 is used for any UV aerosol retrieval that requires an inversion. For example, the value of PAODI using S_1 = 60 and AE = 1.4 is about 200% of PAODI value using S_1 = 35 and AE = 1.4. The furtherer the S_1 deviates goes away from the correct value, the larger the error will be caused for the UVB aerosol retrieval.

$$PAODI_{rel-diff}(\mathrm{i,j}) = \frac{PAODI(i,j) - PAODI_{min}}{PAODI_{min}} \times 100\%. \quad (8)$$

Table 1: The LMOL $S_{1,292}$, HALO $S_{1,532}$ and the HALO AE (292 & 532 nm) for August 2018

Date	Aug. 05		Aug. 06		Aug. 16		Aug. 24		Aug. 28		Aug. 29	
	AM	PM	AM	PM*	AM*	PM	AM	PM	AM	PM	AM	PM*
AE	\	1.7	1.2	1	1	1.1	1.4	1.5	1.6	1.4	1.6	1.4
$S_{1,292}$	\	45	20	20	30	55	40	25	35	35	25	50
$S_{1,532}$	\	48.6	52.1	53.9	62.7	66.7	46.7	49.4	51.7	52.1	46.8	55.5

The selected 292 nm S_1 and AE (292 & 532 nm) were derived from the process mentioned above from all available co-located HALO and LMOL measurements for August 5, 6, 16, 24, 28, and 29 The results and the HALO average S_1 at 532 nm are shown in Table 1. The altitude range for calculating the 292 nm S_1 and AE (292 & 532 nm) are 0.5 to 3 km with exception of the afternoon Aug 6 flight, morning flight of Aug 16, and afternoon flight Aug. 29. In these cases, the altitude range from 0.5 to 2.5 km were used to avoid cloud interferences that prevented proper retrieval and are marked by star on the AM/PM in Table 1.

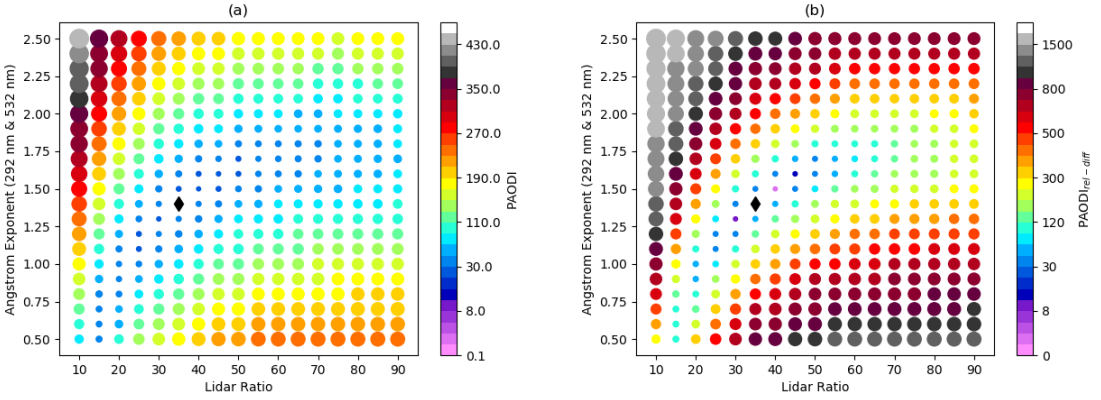

Figure 4: (a) The distribution of PAODI according to the 292 nm S_1 and AE (292 nm & 532 nm). Marker color and size show the value of PAODI. The $PAODI_{min}$ was found and the corresponding S_1 and AE (292 nm & 532 nm) are noted as black diamond. (b) The distribution of $PAODI_{rel-diff}$. Marker size and color show the value of $PAODI_{rel-diff}$. Black diamond shows the minimum value of $PAODI_{rel-diff}$ and represents the ideal point used for optimized 292 nm aerosol retrieval.

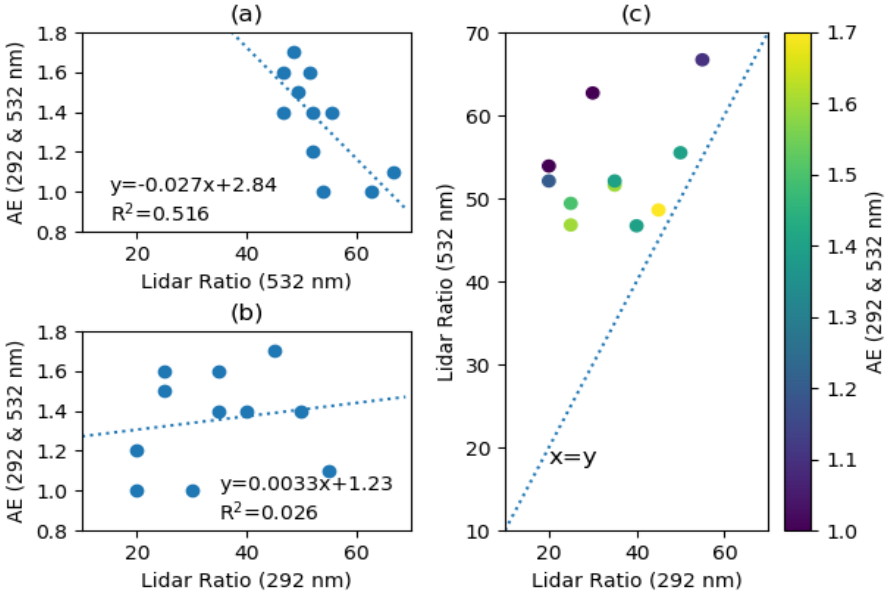

Figure 5: The S_1 for 292 and 532 nm, and the AE (292 & 532 nm) according to Table 1. (a) 532 nm S_1 and AE (292 & 532 nm) (b) 292 nm S_1 and AE (292 & 532) (c) scatter plot of the S_1 for 532 nm and 292 nm with color show the AE (292 & 532 nm).

Figure 5 shows the S_1 and AE for 292 and 532 nm providing a view of the relationships. As shown in Figure 5 (a) and (b), 532 nm S_1 varied between 40 sr and 70 sr and 292 nm S_1 varied between 20 sr and 55 sr with AE (292 & 532 nm) varied from 1 to 1.7. Also, it shows in figure 5 (a) that the 532nm S_1 are anti-correlated with AE (532 & 292 nm) with correlation coefficient

= -0.72 and R square = 0.516. The anti-correlation indicates that the S_1 values dependent on the particle size (Giannakaki et al., 2010). The 292 nm S_1 does not have a clear correlation with AE (532 & 292nm) which is probably caused by the different aerosol absorption characteristic at 292 nm. Figure 5 (c) shows that 292 nm S_1 smaller than 532 nm $S_1$for all cases listed in Table 1. The smaller S_1 at UV wavelength compared with that in visible 532 nm shows the characteristic feature of aged smoke particle (Wandinger et al., 2002; Haarig et al., 2018, Müller et al., 2005; Müller et al., 2007; Ortiz-Amezcua., 2017). This confirms the previous reports that the air parcel arriving northeastern US has passed over active fires in the southeastern US, northwestern US or Columbia British region (Wu et al., 2021; Rogers et al., 2020; Hung et al., 2020).

4 Result

4.1 Comparison of retrieved LMOL Result and HALO aerosol extinction profile

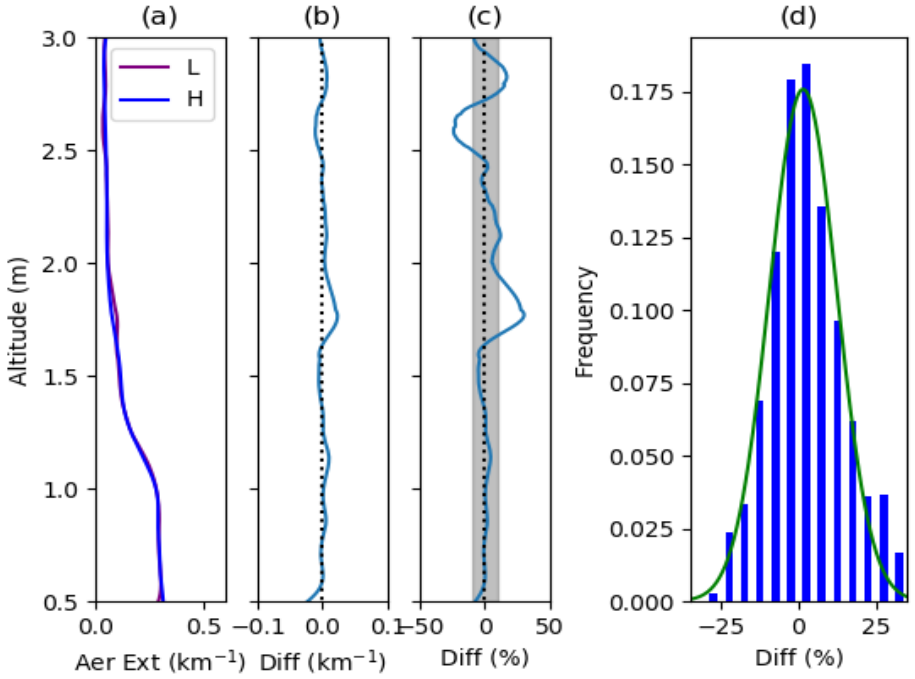

Figure 6: Comparison of the LMOL and HALO derived 292 nm aerosol extinction coefficient on August 28, 2018, afternoon at 13:17 EDT using the S_1 and AE selected in section 3.2. The HALO aerosol extinction profile is converted from 532 nm aerosol extinction product. (a) LMOL and HALO aerosol extinction; (b) difference between LMOL and HALO aerosol extinction; (c) The percent difference between LMOL and HALO aerosol extinction; and (d) The error (percentage difference) probability distribution function for all available comparison between 0.5-2.5 km for August 2018. The width between each bar shows 5% difference.

The optimized 292 nm S_1 and AE (292 & 532 nm) selected in table 1 has corresponding LMOL 292 nm aerosol extinction and 292 nm HALO aerosol profile comparison. The result of LMOL-HALO comparison is shown in figure 6 (a)-(c) for afternoon August 28, 2018. In figure 6 (a), the LMOL 292 nm aerosol extinction profile was shown in purple and HALO aerosol

extinction profile was shown in blue. As shown in figure 6 (c), the percent difference is typically less than 10 % between 0.5 and 3 km. The grey shadow region in the figure 6 (c) show the ±10% region. The percentage difference is larger at higher altitudes because the aerosol concentration is lower above the boundary layer resulting in a larger percentage difference. The percentage difference for all available HALO and LMOL aerosol data between 0.5 to 2.5 km was used to calculate the probability distribution function of the percentage difference for 5% binning. The result in figure 6 (d) shows that the distribution of the frequency is centered about zero and exhibited by a gaussian distribution. The total number of points used for the comparison is 3146. The height of the peak of the distribution function is 0.175 (since it is normalized to 1). The median error percentage is 1.5% with a standard deviation of 11%. These results show that LMOL has the capability to retrieve aerosol extinction in 292nm with reasonable accuracy. This result also provides the aerosol extinction value in the UVB wavelength range which helps to understanding of the UV aerosol optical properties transported wildfire smoke aerosol. This intercomparison is important because it illustrates the ability of the LMOL aerosol retrieval to capture a consistent aerosol feature when compares to HALO, and thus can produce relevant data for campaign analysis in the relationship of aerosols to ozone features.

4.2 Comparisons between LMOL, CCNY lidar, and CL51

To examine the LMOL retrieval beyond those times limited to just the HALO overpasses, the August 28 curtain plot of the LMOL 292 nm aerosol extinction also compared with a co-located Ceilometer CL51 910 nm backscatter signal, and the CCNY lidar (located in NYC) aerosol extinction (converted from 532 nm to 292 nm using AE equal 1.4). This allowed us observe boundary layer development and examine the aerosol variation features during the course of the day. The planetary boundary layer (PBL) height increases after 10 am EDT and reaches a maximum at 17 EDT. The comparison between the CCNY aerosol extinction and the LMOL aerosol extinction shows that retrieved LMOL UV aerosol extinction are qualitatively consistent. The difference of the aerosol extinction between the LMOL and CCNY measurement probably caused by the atmosphere variation in different locations with about 60 km distance. The PBL height was retrieved by applying a wavelet method to the LMOL and CCNY aerosol data (Brooks et al., 2003; Compton et al., 2013; Scarino et al., 2014). PBL height of the ceilometer was obtained from the CL51 data product which could be obtained from the LISTOS archive data. PBL height were overplotted on the aerosol and O_3 curtain plot in figure 7 (a) - (d). LMOL retrieved UVB aerosol extinction, and co-located CL51 aerosol backscatter show exactly same variation for the PBL evolution except the higher backscatter between 12 to 14 EDT. That is because that cloud screen process was applied to the LMOL UVB aerosol retrieval process. This intercomparison is important because it illustrates the ability of the LMOL aerosol retrieval to capture a consistent aerosol feature when compares to other lidar systems and thus can produce relevant data for campaign analysis in the relationship of aerosols to ozone features. Capturing aerosol extinction between 0.5 to 3.0 km is very useful because it will help us to retrieve the PBL height and help us to learn aerosol property in the lower part of troposphere. Furthermore, aerosol profiling information can still play an important role for model intercomparisons and satellite retrievals.

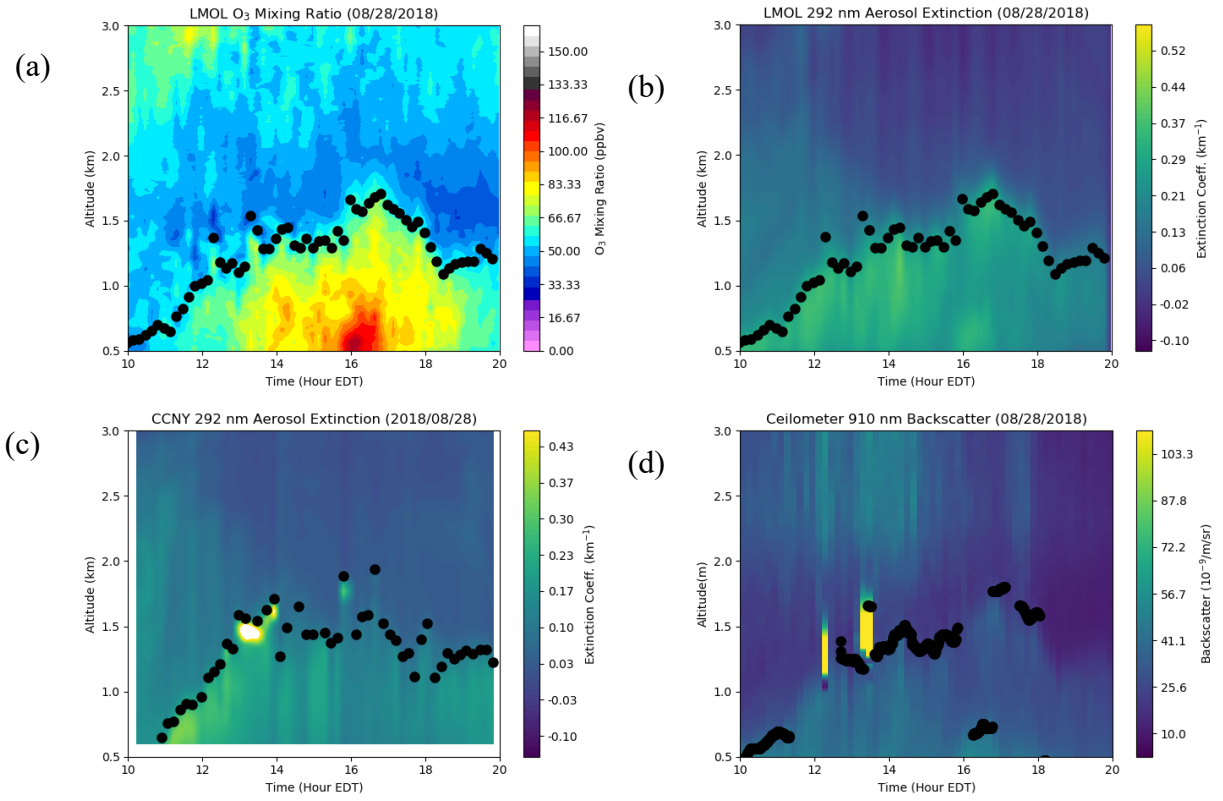

Figure 7. (a) The O_3 variation on August 28, 2018 (b) Retrieved LMOL UVB aerosol extinction coefficient curtain plot on August 28, 2018 (c) Same day CCNY lidar aerosol extinction coefficient (converted to 292 nm). (d) Same day 910nm ceilometer CL51 (same location as LMOL) backscatter. The black dot on the curtain plot of (b), (c), and (d) show the planetary boundary layer (PBL) height.

5 Uncertainty

The sensitivity of the algorithm to uncertainty in the input parameters is analyzed for August 28, 2018 case in this section. The aerosol extinction retrieval uncertainties caused by the lidar detection noise, reference value estimation, atmospheric molecular density, ozone concentration uncertainty, and the S_1 will be discussed in this section. The quantitative estimation of the aerosol extinction and backscatter uncertainty is challenging, and no standardized recommendation exists (Leblanc et al., 2016b). In this work, the total uncertainty of the retrieved extinction coefficient is calculated by following standard propagation of error practices. The retrieved aerosol profile depends on several instrumental and physical parameters for the lidar system. The measurement model for the system is presented as equation (9). The individual values y of the quantity Y was shown in equation (10) (Leblanc et al., 2016b).

$$Y = f(X_1, X_2, X_3, \ldots, X_N) \quad (9)$$

$$y = f(x_1, x_2, x_3, \dots, x_N) = y_0 + \sum_{n=1}^{N} \frac{\partial y}{\partial x_n} x_n \quad (10)$$

The combined standard uncertainty u_y is obtained using the individual standard measurement uncertainties associated with the input quantities in the equation (9). As shown in equation (11), the combined standard uncertainty u_y equals the positive squared root of the combined variance in case of all variables that are independent (Leblanc et al., 2016b).

$$u_y^2 = \sum_{n=1}^{N} \left(\frac{\partial y}{\partial x_n}\right)^2 u_n^2 \quad (11)$$

As shown in section 2, the signal was used to calculate the aerosol extinction noted as $X(R)$ and shown as equation (12).

$$X(R) = [P(R) - P_0]R^2 \exp\left[2 \int_0^R \sigma_{O_3} N_{O_3}(r)\, dr\right] \quad (12)$$

The detection noise uncertainty is derived from Poisson statistics associated with probability of detection of a repeated random event. Following Leblanc et al., 2016b, the subscript (DET) was used for detection noise. The uncertainty in the raw signal $P(R)$ caused by detection noise could be expressed as equation (13) and reflect purely random effects during detection (Russell et al., 1979).

$$u_{P(DET)}(R) = \sqrt{P(R)} \quad (13)$$

It is propagated to the background and O_3 corrected signal $X(R)$ by apply equation (11) to equation (12):

$$u_{X(DET)}(R) = R^2 \exp\left[2 \int_0^R \sigma_{O_3} N_{O_3}(r)\, dr\right] \sqrt{P(R)} \quad (14)$$

Similarly, the O_3 uncertainty is noted as u_{o_3} , and it is propagated to the background and O_3 corrected signal $X(R)$as show in equation (15):

$$u_{X(O_3)}(R) = \frac{\partial X(R)}{\partial O_3(R)} u_{o_3} \quad (15)$$

The propagated uncertainty caused by detection noise and O_3 could be got by apply equation (11) to equation (4):

$$u_{\alpha_1(DET)}(R) = \frac{\partial \alpha_1(R)}{\partial X(R)}\, u_{X(DET)}(R) \quad (16)$$

$$u_{\alpha_1(O_3)}(R) = \frac{\partial \alpha_1(R)}{\partial X(R)}\, u_{X(O_3)}(R) \quad (17)$$

So, the total uncertainty shows as equation (18):

$$u_{\alpha_1}(R) = \sqrt{\left(\frac{\partial \alpha_1(R)}{\partial X(R)} u_{\alpha_1(DET)}(R)\right)^2 + \left(\frac{\partial \alpha_1(R)}{\partial X(R)} u_{\alpha_1(O_3)}(R)\right)^2 + \left(\frac{\partial \alpha_1(R)}{\partial \beta_2(R)} u_{\alpha_1(N_m)}(R)\right)^2 + \left(\frac{\partial \alpha_1(R)}{\partial S_1(R)} u_{\alpha_1(S_1)}(R)\right)^2 + \left(\frac{\partial \alpha_1(R)}{\partial \alpha_1(R_c)} u_{\alpha_1\left(\alpha_{1(R_c)}\right)}(R)\right)^2} \quad (18)$$

The uncertainty shows in equation (18) consider the impact of integral uncertainty from targeted altitude to the reference point because the equation (4) has the integral taking account the molecular extinction and the O_3 corrected return lidar signal of the target altitude to the reference point. The $u_{\alpha_1(N_m)}(R)$ is the atmospheric molecular number density uncertainty we use as 1% following the result from Kuang et al., 2020. The S_1 is assigned 35 ± 15 for this example and the uncertainty of the $u_{\alpha_1(S_1)}(R)$ is about $\pm 40\%$. The uncertainty for the reference value is taken as 10 times for the total uncertainty analysis as show in equation (18).

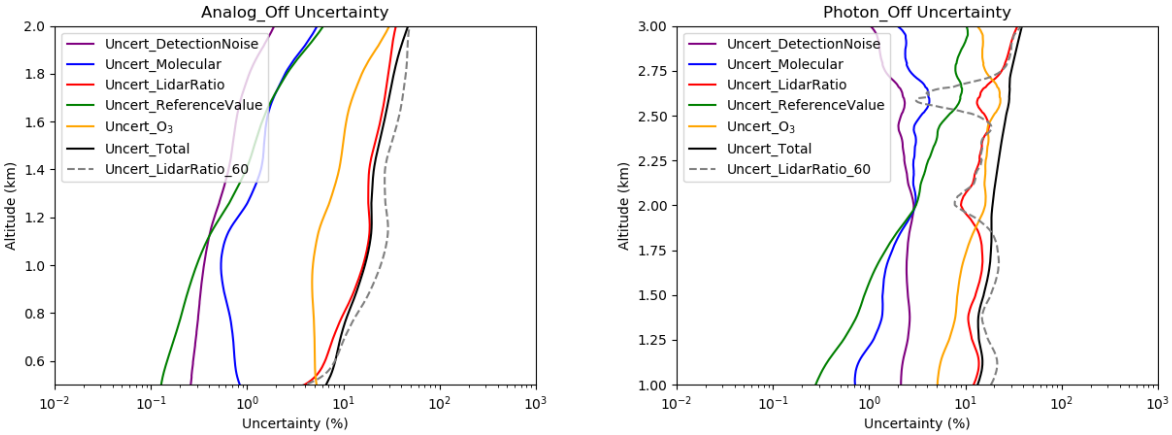

Figure 8: The uncertainty budget for the LMOL Analog channel (left) and the Photon channel (right) for August 28, 2018 afternoon retrieval. The uncertainties are attributed to different factors: detection noise (purple), molecular number density (blue), S_1 (red), reference value (green), uncertainty of O_3 (orange), total uncertainty (black). The uncertainty caused by using 60 sr as S_1 was shown in dashed gray line.

We calculate uncertainties of the analog channel and the photon channel separately, so we could assess how the different parameters impact the retrieval uncertainty for both channels. The photocurrent for the PMT analog mode no longer follows strick Poisson distribution, but there still may be a quantitative estimate of this uncertainty. The uncertainty for detection noise for the PMT analog channel are recalculated using the method mentioned in Liu 2006 et al and result is shown in left one in figure 8. As figure 8 shown, the uncertainty caused by detection noise is small for both channels. The uncertainty caused by the reference value and the molecular are less than 10% for both channels. Ozone uncertainty are 10% for the LMOL system and cause mostly less than 20% uncertainty for the analog channel and photon channel. The uncertainty of the S_1 cause about

4%-30% uncertainty for both analog and photon channel. The uncertainty of the S_1 and O_3 dominate the total uncertainty for both channels. We also show the uncertainty caused by using 60 sr as S_1 for UVB aerosol retrieval for afternoon August 28, 2018. It shows that S_1 equals 60 will increase aerosol retrieval uncertainty in PBL but uncertainty didn't change much above 2 km except in a layer located at 2.6 km.

6 Conclusion

For the first time, the aerosol extinction coefficient profiles, retrieved from the LMOL 292nm attenuated backscatter using the Fernald algorithm, are compared with airborne HALO data. A partial AOD difference method was introduced to determine the optimized value for 292 nm S_1 and AE (292& 532nm) from these instruments. The optimized S_1 and AE (292& 532nm) improved the accuracy of the UVB aerosol retrieval. In addition, the knowledge of these parameters can improve our understanding of the aerosol properties; as an example, the case studies in the present paper demonstrated that we were in presence of transported smoke. The inter-comparison between HALO and LMOL aerosol products showed an agreement within 10% up to 3 km after the optimization method was applied in the case of August 28, 2018. The retrieved LMOL 292 nm aerosol was also compared with co-located ceilometer and CCNY aerosol lidar. It shows that LMOL could capture a consistent aerosol feature and mixing layer evolution. Error analysis shows that the uncertainty from O_3 and S_1 dominate the 292 nm aerosol retrieval and needs to be carefully considered in the retrievals of aerosol profiles of all the TOLNET Lidars. In cases when there is no HALO data, a-priori determinations from differing aerosol types based on this kind of analysis work will serve to provide reasonable S_1. Consequently, further research is needed to characterize S_1 and AE at UVB wavelengths: first, an effort should be made on determining the variation of S_1 and AE with altitude by carefully addressing the uncertainties in the HALO S_1 profile products; second, additional co-located LMOL/HSRL measurements should be done to evaluate S_1 and AE for different aerosol types (smoke, dust, marine aerosol, and pollutant aerosol). This characterization could ultimately enable the use of equipment with a better availability than an HSRL (examples of such equipment could be the MPLs) to provide the ancillary data necessary for the aerosol extinction retrieval.

Data availability. The LMOL O_3 raw data used in this study can be downloaded from the LMOL website: https://www-air.larc.nasa.gov/missions/TOLNet/. The LMOL O_3 used to correct the raw data can be download from the TOLnet website:https://www-air.larc.nasa.gov/cgi-bin/ArcView.1/TOLNet?NASA-LARC=1#0. The HALO aerosol backscatter/extinction data used in this work can be downloaded from the LISTOS website: https://www-air.larc.nasa.gov/cgi-bin/ArcView/listos.

Author contributions

LL and TB formulated the overarching research goals. GG supported the O_3 data analysis which is a key factor for the aerosol retrieval algorithm and plot the figure 1 for the flow chart for approach used in this work. LL and JS did the UV aerosol extinction retrieval calculation. LL did S_1 and AE determination, aerosol extinction comparison between LMOL and HALO. AN provide HALO aerosol data product and HALO instrument introduction in paper. YW and FM involve in CCNY lidar aerosol data and provide CCNY PBL height data. SK contributes to the UV aerosol retrieval algorithm. LL wrote the initial draft of the paper with contributions from all co-authors. All authors reviewed the manuscript.

Competing interests

The authors declare that they have no conflict of interest.

Acknowledgement

The authors gratefully acknowledge support by the NASA Postdoctural Program that enabled this study. LMOL and HALO lidar participation in the LISTOS campaign was made possible with funding by the NASA Tropospheric Composition Program. We gratefully acknowledges William Carrion and Joseph Sparrow for LMOL operational support and the Connecticut Department of Energy and Environmental Protection for providing site support to enable LMOL operations at the Westport location. The HALO team acknowledges support from the Langley Research Center Research Services Division for the operation and maintenance of the King Air B200 Aircraft throughout the duration of the LISTOS campaign. We thank Susan Kooi and James Collins for their contribution to analysis and archival of the HALO HSRL dataset. We thank Daniel B. Phoenix for his valuable comments and his help in editing the manuscript. Y.W. and F. M. are supported by the New York State Energy Resources Development Authority (grant # 137482), NESCAUM (grant # 2411) and NOAA-CESSRST under the Cooperative Agreement Grant # NA16SEC4810008.

References

Aggarwal, M., Whiteway, J., Seabrook, J., Gray, L., Strawbridge, K., Liu, P., O'Brien, J., Li, S.-M., and McLaren, R.: Airborne lidar measurements of aerosol and ozone above the Canadian oil sands region, Atmos. Meas. Tech., 11, 3829–3849, https://doi.org/10.5194/amt-11-3829-2018, 2018.

Andreae, M. O. and Merlet, P.: Emission of trace gases and aerosols from biomass burning, Global Biogeochem. Cy., 15, 955–966,https://doi.org/10.1029/2000GB001382, 2001.

Bais, A. F., Zerefos, C. S., Meleti, C., Ziomas, I. C., and Tourpali, K.: Spectral measurements of solar UVB radiation and its relations to total ozone, SO_2, and clouds, J. Geophys. Res.-Atmos., 98, 5199–5204, https://doi.org/10.1029/92jd02904, 1993.

Berkoff, T., Gronoff, G., Sullivan, J., Nino, L., Carrion, W., Twigg, L., ... & Szykman, J. (2018). Ozone Lidar Observations During the Long Island Sound Tropospheric Ozone Study.

Browell, E. V., Ismail, S., and Shipley, S. T.: Ultraviolet DIAL measurements of O_3 profiles in regions of spatially inhomogeneous aerosols, Appl. Opt., 24, 2827–2836, https://doi.org/10.1364/ao.24.002827, 1985.

Brooks, I. M.: Finding Boundary Layer Top: Application of a Wavelet Covariance Transform to Lidar Backscatter Profiles, J. Atmos. Ocean. Tech., 20, 1092–1105, https://doi.org/10.1175/1520-0426(2003)020<1092:fbltao>2.0.co;2, 2003.

Burton, S. P., Ferrare, R. A., Hostetler, C. A., Hair, J. W., Kittaka, C., Vaughan, M. A., Obland, M. D., Rogers, R. R., Cook, A. L., Harper, D. B., and Remer, L. A.: Using Airborne High Spectral Resolution Lidar Data to Evaluate Combined Active Plus Passive Retrievals of Aerosol Extinction Profiles, J. Geophys. Res., 115, D00H15, https://doi.org/10.1029/2009JD012130, 2010.

Burton, S. P., Ferrare, R. A., Hostetler, C. A., Hair, J. W., Rogers, R. R., Obland, M. D., Butler, C. F., Cook, A. L., Harper, D. B., and Froyd, K. D.: Aerosol classification using airborne High Spectral Resolution Lidar measurements – methodology and examples, Atmos. Meas. Tech., 5, 73–98, https://doi.org/10.5194/amt-5-73-2012, 2012.

Burton, S. P., Ferrare, R. A., Vaughan, M. A., Omar, A. H., Rogers, R. R., Hostetler, C. A., and Hair, J. W.: Aerosol classification from airborne HSRL and comparisons with the CALIPSO vertical feature mask, Atmos. Meas. Tech., 6, 1397–1412, https://doi.org/10.5194/amt-6-1397-2013, 2013.

Burton, S. P., Vaughan, M. A., Ferrare, R. A., and Hostetler, C. A.: Separating mixtures of aerosol types in airborne High Spectral Resolution Lidar data, Atmos. Meas. Tech., 7, 419–436, https://doi.org/10.5194/amt-7-419-2014, 2014.

Burton, S. P., Hair, J. W., Kahnert, M., Ferrare, R. A., Hostetler, C. A., Cook, A. L., Harper, D. B., Berkoff, T. A., Seaman, S. T., Collins, J. E., Fenn, M. A., and Rogers, R. R.: Observations of the spectral dependence of linear particle depolarization ratio of aerosols using NASA Langley airborne High Spectral Resolution Lidar, Atmos. Chem. Phys., 15, 13453–13473, https://doi.org/10.5194/acp-15-13453-2015, 2015.

Carlund, T., Kouremeti, N., Kazadzis, S., and Gröbner, J.: Aerosol optical depth determination in the UV using a four-channel precision filter radiometer, Atmos. Meas. Tech., 10, 905–923, https://doi.org/10.5194/amt-10-905-2017, 2017.

Compton, J. C., Delgado, R., Berkoff, T. A., and Hoff, R. M.: Determination of planetary boundary layer height on short spatial and temporal scales: a demonstration of the covari- ance wavelet transform in ground-based wind profiler and lidar measurements, J. Atmos. Ocean. Tech., 30, 1566–1575, https://doi.org/10.1175/JTECH-D-12-00116.1, 2013.

Cottle, P., Strawbridge, K., & McKendry, I.: Long-range transport of Siberian wildfire smoke to British Columbia: Lidar observations and air quality impacts. Atmos. Environ., *90*, 71-77, doi:10.1016/j.atmosenv.2014.03.005, 2014.

Dacic, N., Sullivan, J. T., Knowland, K. E., Wolfe, G. M., Oman, L. D., Berkoff, T. A., & Gronoff, G. P.: Evaluation of NASA's high-resolution global composition simulations: Understanding a pollution event in the Chesapeake Bay during the summer 2017 OWLETS campaign. Atmos. Environ., *222*, 117133, doi:10.1016/j.atmosenv.2019.117133, 2020.

De Young, R., Carrion, W., Ganoe, R., Pliutau, D., Gronoff, G., Berkoff, T., and Kuang, S.: Langley mobile ozone lidar: ozone and aerosol atmospheric profiling for air quality research, Appl. Opt., 56, 721–730, https://doi.org/10.1364/ao.56.000721, 2017.

Dreessen, J., Sullivan, J., and Delgado, R.: Observations and impacts of transported Canadian wildfire smoke on ozone and aerosol air quality in the Maryland region on June 9–12, 2015, J. Air Waste Manage Assoc., 66, 842–862, https://doi.org/10.1080/10962247.2016.1161674, 2016.

Farris, B. M., Gronoff, G. P., Carrion, W., Knepp, T., Pippin, M., and Berkoff, T. A.: Demonstration of an off-axis parabolic receiver for near-range retrieval of lidar ozone profiles, Atmos. Meas. Tech. Discuss., https://doi.org/10.5194/amt-2018-178, 2019.

Fernald, F. G., Herman, B. M., and Reagan, J. A.: Determination of aerosol height distributions with lidar, J. Appl. Meteorol., 11, 482–489, https://doi.org/10.1175/1520-0450(1972)011<0482:DOAHDB>2.0.CO;2, 1972.

Fernald, F. G.: Analysis of atmospheric lidar observations: some comments, Appl. Optics, 23, 652–653, https://doi.org/10.1364/AO.23.000652, 1984.

Giannakaki, E., Balis, D. S., Amiridis, V., and Zerefos, C: Optical properties of different aerosol types: seven years of combined Raman-elastic backscatter lidar measurements in Thessaloniki, Greece, Atmos. Meas. Tech., 3, 569–578, https://doi.org/10.5194/amt-3-569-2010, 2010.

Gronoff, G., Robinson, J., Berkoff, T., Swap, R., Farris, B., Schroeder, J., Halliday, H. S., Knepp, T., Spinei, E., Carrion, W., and Adcock, E. E.: A method for quantifying near range point source induced O3 titration events using Co-located Lidar and Pandora measurements, Atmos. Environ., 204, 43–52, doi:10.1016/j.atmosenv.2019.01.052, 2019.

Gronoff, G., Berkoff, T., Knowland, K., E., Lei, L., Shook, M., Fabbri, B., Carrion, W., and Langford, A.: Case study of stratospheric Intrusion above Hampton, Virginia: lidar-observation and modeling analysis. Atmos. Environ., 118498, https://doi.org/10.1016/j.atmosenv.2021.118498, 2021.

Haarig, M., Ansmann, A., Baars, H., Jimenez, C., Veselovskii, I., Engelmann, R., and Althausen, D.: Depolarization and lidar ratios at 355, 532, and 1064 nm and microphysical properties of aged tropospheric and stratospheric Canadian wildfire smoke, Atmos. Chem. Phys., 18, 11847–11861, https://doi.org/10.5194/acp-18-11847-2018, 2018.

Hair, J. W., Hostetler, C. A., Cook, A. L., Harper, D. B., Ferrare, R. A., Mack, T. L., Welch, W., Izquierdo, L. R., and Hovis, F. E.: Airborne High Spectral Resolution Lidar for profiling aerosol optical properties, Appl. Optics, 47, 6734–6752, https://doi.org/10.1364/AO.47.006734, 2008.

Jin, Y., Kai, K., Kawai, K., Nagai, T., Sakai, T., Yamazaki, A., Uchiyama, A., Batdorj, D., Sugimoto, N., and Nishizawa, T.: Ceilometer calibration for retrieval of aerosol optical properties, J. Quant. Spectrosc. Ra., 153, 49–56, https://doi.org/10.1016/j.jqsrt.2014.10.009, 2015.

Hung, W. T., Lu, C. H. S., Shrestha, B., Lin, H. C., Lin, C. A., Grogan, D., ... & Joseph, E.: The impacts of transported wildfire smoke aerosols on surface air quality in New York State: A case study in summer 2018. Atmos. Environ., 227, 117415, https://doi.org/10.1016/j.atmosenv.2020.117415, 2020.

Kovalev, V. A. and Eichinger, W. E.: Elastic Lidar Theory, Practice, and Analysis Methods, John Wiley & Sons, Inc., New Jersey, USA, DOI:10.1002/0471643173, 2004.

Kuang, S., Wang, B., Newchurch, M. J., Knupp, K., Tucker, P., Eloranta, E. W., Garcia, J. P., Razenkov, I., Sullivan, J. T., Berkoff, T. A., Gronoff, G., Lei, L., Senff, C. J., Langford, A. O., Leblanc, T., and Natraj, V.: Evaluation of UV aerosol retrievals from an ozone lidar, Atmos. Meas. Tech., 13, 5277–5292, https://doi.org/10.5194/amt-13-5277-2020, 2020.

Leblanc, T., Sica, R. J., van Gijsel, J. A. E., Godin-Beekmann, S., Haefele, A., Trickl, T., Payen, G., and Gabarrot, F.: Proposed standardized definitions for vertical resolution and uncertainty in the NDACC lidar ozone and temperature algorithms – Part 1: Vertical resolution, Atmos. Meas. Tech., 9, 4029–4049, https://doi.org/10.5194/amt-9-4029-2016, 2016a.

Leblanc, T., Sica, R. J., van Gijsel, J. A. E., Godin-Beekmann, S., Haefele, A., Trickl, T., Payen, G., and Liberti, G.: Proposed standardized definitions for vertical resolution and uncertainty in the NDACC lidar ozone and temperature algorithms – Part 2: Ozone DIAL uncertainty budget, Atmos. Meas. Tech., 9, 4051–4078, https://doi.org/10.5194/amt-9-4051-2016, 2016b.

Leblanc, T., Brewer, M. A., Wang, P. S., Granados-Muñoz, M. J., Strawbridge, K. B., Travis, M., Firanski, B., Sullivan, J. T., McGee, T. J., Sumnicht, G. K., Twigg, L. W., Berkoff, T. A., Carrion, W., Gronoff, G., Aknan, A., Chen, G., Alvarez, R. J., Langford, A. O., Senff, C. J., Kirgis, G., Johnson, M. S., Kuang, S., and Newchurch, M. J.: Validation of the TOLNet lidars: the Southern California Ozone Observation Project (SCOOP), Atmos. Meas. Tech., 11, 6137–6162, https://doi.org/10.5194/amt-11-6137-2018, 2018.

Lee, S., Hwang, S. O., Kim, J., and Ahn, M. H.: Characteristics of cloud occurrence using ceilometer measurements and its re- lationship to precipitation over Seoul, Atmos. Res., 201, 46–57, https://doi.org/10.1016/j.atmosres.2017.10.010, 2018.

Li H, Chang J, Xu F, Liu B, Liu Z, Zhu L, Yang Z. An RBF neural network approach for retrieving atmospheric extinction coefficients based on lidar measurements, **Appl**. Phys. B, 124(9):1-8. https://doi.org/10.1007/s00340-018-7055-1, 2018.

Liu, Z., Hunt, W., Vaughan, M., Hostetler, C., McGill, M., Powell, K.,Winker, D., and Hu, Y.: Estimating random errors due to shot noise in backscatter lidar observations, Appl. Optics, 45, 4437– 4447, 2006.

Lopes, F. J. S., Landulfo, E., and Vaughan, M. A.: Evaluating CALIPSO's 532 nm lidar ratio selection algorithm using AERONET sun photometers in Brazil, Atmos. Meas. Tech., 6, 3281–3299, https://doi.org/10.5194/amt-6-3281-2013, 2013.

Moozhipurath, R. K., Kraft, L., & Skiera, B.: Evidence of protective role of Ultraviolet-B (UVB) radiation in reducing COVID-19 deaths. *Sci Rep* **10,** 17705, https://doi.org/10.1038/s41598-020-74825-z, 2020.

Müller, D., Mattis, I., Wandinger, U., Ansmann, A., Al- thausen, D., and Stohl, A.: Raman lidar observations of aged Siberian and Canadian forest fire smoke in the free troposphere over Germany in 2003: microphysical particle characterization, J. Geophys. Res., 110, D17201, https://doi.org/10.1029/2004JD005756, 2005.

Müller, D., Ansmann, A., Mattis, I., Tesche, M., Wandinger, U., Althausen, D. and Pisani, G.: Aerosol-type-dependent lidar ratios observed with Raman lidar, J. Geophys. Res., 112, D16202, https://doi.org/10.1029/2006JD008292, 2007.

Nehrir, A. R., Kiemle, C., Lebsock, M. D., Kirchengast, G., Buehler, S. A., Löhnert, U., Liu, C.-L., Hargrave, P. C., Barrera-Verdejo, M., and Winker, D. M.: Emerging Technologies and Synergies for Airborne and Space-Based Measurements of Water Vapor Profiles, Surv. Geophys., 38, 1445–1482, https://doi.org/10.1007/s10712-017-9448-9, 2017.

Nicolae, D., Nemuc, A., Müller, D., Talianu, C., Vasilescu, J., Belegante, L., and Kolgotin, A.: Characterization of fresh and aged biomass burning events using multiwavelength Raman lidar and mass spectrometry, J. Geophys. Res.-Atmos., 118, 2956–2965, https://doi.org/10.1002/jgrd.50324, 2013.

Omar, A. H., Winker, D. M., Vaughan, M. A., Hu, Y., Trepte, C. R., Ferrare, R. A., Lee, K. P., Hostetler, C. A., Kittaka, C., Rogers, R. R., and Kuehn, R. E.: The CALIPSO Automated Aerosol Classification and Lidar Ratio Selection Algorithm, J. Atmos. Ocean. Tech., 26, 1994–2014, https://doi.org/10.1175/2009JTECHA1231.1, 2009.

Ortiz-Amezcua, P., Guerrero-Rascado, J. L., Granados-Muñoz, M. J., Benavent-Oltra, J. A., Böckmann, C., Samaras, S., Stachlewska, I. S., Janicka, L., Baars, H., Bohlmann, S., and Alados- Arboledas, L.: Microphysical characterization of long-range transported biomass burning particles from North America at three EARLINET stations, Atmos. Chem. Phys., 17, 5931–5946, https://doi.org/10.5194/acp-17-5931-2017, 2017.

Phuleria, H. C., Fine, P. M., Zhu, Y. F., and Sioutas, C.: Air quality impacts of the October 2003 Southern California wildfires, J. Geophys. Res., 110, D07S20–D07S20, https://doi.org/10.1029/2004JD004626, 2005.

Reid, J. S., Koppmann, R., Eck, T. F., and Eleuterio, D. P.: A review of biomass burning emissions part II: intensive physical properties of biomass burning particles, Atmos. Chem. Phys., 5, 799–825, https://doi.org/10.5194/acp-5-799-2005, 2005.

Rogers, H. M., Ditto, J. C., and Gentner, D. R.: Evidence for impacts on surface-level air quality in the northeastern US from long-distance transport of smoke from North American fires during the Long Island Sound Tropospheric Ozone Study (LISTOS) 2018, Atmos. Chem. Phys., 20, 671–682, https://doi.org/10.5194/acp-20-671-2020, 2020.

Russell, P. B., Swissler, T. J., and McCormick, M. P.: Methodology for error analysis and simulation of lidar aerosol measurements, Appl. Optics, 18, 3783–3797, https://doi.org/10.1364/AO.18.003783, 1979.

Sasano, Y. and Nakane, H.: Significance of the extinction/backscatter ratio and the boundary value term in the solution for the two-component lidar equation, Appl. Opt., 23, 1–13, https://doi.org/10.1364/AO.23.0011_1, 1984.

Sasano, Y., Browell, E. V., and Ismail, S.: Error caused by using a constant extinction/backscattering ratio in the lidar solution, Appl. Opt., 24, 3929–3932, https://doi.org/10.1364/AO.24.003929, 1985.

Scarino, A. J., Obland, M. D., Fast, J. D., Burton, S. P., Fer- rare, R. A., Hostetler, C. A., Berg, L. K., Lefer, B., Haman, C., Hair, J. W., Rogers, R. R., Butler, C., Cook, A. L., and Harper, D. B.: Comparison of mixed layer heights from airborne high spectral resolution lidar, ground-based measurements, and the WRF-Chem model during CalNex and CARES, Atmos. Chem. Phys., 14, 5547–5560, https://doi.org/10.5194/acp-14- 5547-2014, 2014.

Wandinger, U., Müller, D., Böckmann, C., Althausen, D., Matthias, V., Bösenberg, J, Weiß, V., Fiebig, M., Wendisch, M., Stohl, A., and Ansmann, A.: Optical and microphysical characterization of biomass-burning and industrial-pollution aerosols from multiwavelength lidar and aircraft measurements, J. Geophys. Res., 107, 8125, https://doi.org/10.1029/2000JD000202, 2002.

Schoennagel, T., Balch, J. K., Brenkert-Smith, H., Dennison, P. E., Harvey, B. J., Krawchuk, M. A., Mietkiewicz, N., Morgan, P., Moritz, M. A., Rasker, R., Turner, M. G., and Whitlock, C.: Adapt to more wildfire in western North American forests as climate changes, P. Natl. Acad. Sci. USA, 114, 4582–4590, https://doi.org/10.1073/pnas.1617464114, 2017.

Strawbridge, K. B., Travis, M. S., Firanski, B. J., Brook, J. R., Staebler, R., and Leblanc, T.: A fully autonomous ozone, aerosol and nighttime water vapor lidar: a synergistic approach to profiling the atmosphere in the Canadian oil sands region, Atmos. Meas. Tech., 11, 6735–6759, https://doi.org/10.5194/amt-11-6735-2018, 2018.

Sugimoto, N. and Lee, C. H.: Characteristics of dust aerosols in- ferred from lidar depolarization measurements at two wavelengths, Appl. Optics, 45, 7468–7474, 2006.

Sullivan, J. T., Berkoff, T., Gronoff, G., Knepp, T., Pippin, M., Allen, D., Twigg, L., Swap, R., Tzortziou, M., Thompson, A. M., Stauffer, R. M., Wolfe, G. M., Flynn, J., Pusede, S. E., Judd, L. M., Moore, W., Baker, B. D., Al-Saadi, J., and McGee, T. J.: The Ozone Water–Land Environmental Transition Study: An Innovative Strategy for Understanding Chesapeake Bay Pollution Events, B. Am. Meteorol. Soc., 100, 291–306, https://doi.org/10.1175/BAMS-D-18-0025.1, 2019.

Wang, Y., Zhao, C., Dong, Z., Li, Z., Hu, S., Chen, T., ... & Wang, Y.: Improved retrieval of cloud base heights from ceilometer using a non-standard instrument method. Atmos. Res., *202*, 148-155.doi: 10.1016/j.atmosres.2017.11.021, 2018.

Wagner, F. and Silva, A. M.: Some considerations about Ångström exponent distributions, Atmos. Chem. Phys., 8, 481–489, https://doi.org/10.5194/acp-8-481-2008, 2008.

Wu, Y., Arapi, A., Huang, J., Gross, B., and Moshary, F.: Intra-continental wildfire smoke transport and impact on local air quality observed by ground-based and satellite remote sensing in New York City, Atmos. Environ., 187, 266–281, https://doi.org/10.1016/j.atmosenv.2018.06.006, 2018.

Wu, Y., Zhao, K., Huang, J., Arend, M., Gross, B., and Moshary, F.: Observation of heat wave effects on the urban air quality and PBL in New York City area, Atmos. Environ., *218*, 117024, https://doi.org/10.1016/j.atmosenv.2019.117024, 2019.

Wu, Y., Nehrir, A. R., Ren, X., Dickerson, R. R., Huang, J., Stratton, P. R., Gronoff G., Kooi S. A., Collins J. E., Beroff T. A., Lei L., Gross B., and Moshary, F.: Synergistic aircraft and ground observations of transported wildfire smoke and its impact on air quality in New York City during the summer 2018 LISTOS campaign. Science of The Total Environment, 773, 145030, https://doi.org/10.1016/j.scitotenv.2021.145030, 2021.

Young, S. A.: Analysis of lidar backscatter profiles in optically thin clouds, Appl. Opt., 34, 7019–7031, https://doi.org/10.1364/AO.34.007019, 1995.

Young, S. A. and Vaughan, M. A.: The retrieval of profiles of particulate extinction from Cloud Aerosol Lidar Infrared Pathfinder Satellite Observations (CALIPSO) data: Algorithm description, J. Atmos. Ocean. Tech., 26, 1105–1119, https://doi.org/10.1175/2008JTECHA1221.1, 2009.

Zauscher, M. D., Wang, Y., Moore, M. J. K., Gaston, C. J., and Prather, K. A.: Air Quality Impact and Physicochem- ical Aging of Biomass Burning Aerosols during the 2007 San Diego Wildfires, Environ. Sci. Technol., 47, 7633–7643, https://doi.org/10.1021/es4004137, 2013.

Zoogman, P., Liu, X., Suleiman, R., Pennington, W., Flittner, D., Al-Saadi, J., Hilton, B., Nicks, D., Newchurch, M., Carr, J., Janz, S., Andraschko, M., Arola, A., Baker, B., Canova, B., Miller,C. C., Cohen, R., Davis, J., Dussault, M., Edwards, D., Fishman, J., Ghulam, A., Abad, G. G., Grutter, M., Herman, J., Houck, J., Jacob, D., Joiner, J., Kerridge, B., Kim, J., Krotkov, N., Lamsal, L., Li, C., Lindfors, A., Martin, R., McElroy, C., McLinden, C., Natraj, V., Neil, D., Nowlan, C., O'Sullivan, E.,

Palmer, P., Pierce, R., Pippin, M., Saiz-Lopez, A., Spurr, R., Szykman, J., Torres, O., Veefkind, J., Veihelmann, B., Wang, H., Wang, J., and Chance, K.: Tropospheric emissions: Monitoring of pollution (TEMPO), J. Quant. Spectrosc. Ra., 186, 17–39, https://doi.org/10.1016/j.jqsrt.2016.05.008, 2017.